

riiness due to the formation of solid solution. With lower magnesia content a liquid phase appears that causes wetting and penetration between the grains of the refractory to take place, eventually leading to failure. On the other hand, with chrome-magnesite bricks, the higher the Cr_2O_3 content the higher is the corrosion resistance due to formation of the refractory $\text{Cu}_2\text{O}\cdot\text{Cr}_2\text{O}_3$ and its growth as interlocking laths in the liquid phase.

Registry No. CuO, 1317-38-0; periclase, 1317-74-4; gugganite, 67164-58-3; chromium copper oxide, 12017-79-7.

Literature Cited

Alper, A. M.; McNally, R. N.; Doman, R. C.; Keihn, F. G. *J. Am. Ceram. Soc.* **1964**, *47*, 30.

Drenkhahn, H.; Mueller-Bouchbaum, H. K. *Z. Anorg. Allg. Chem.* **1975**, *418*, 116.
Gadalla, A. M.; Ford, W. F.; White, J. *Trans. Br. Ceram. Soc.* **1963**, *62*, 54.
Gadalla, A. M.; White, J. *Trans. Br. Ceram. Soc.* **1964**, *63*, 39.
Gadalla, A. M.; White, J. *Trans. Br. Ceram. Soc.* **1964b**, *63*, 119.
Gadalla, A. M.; White, J. *Trans. Br. Ceram. Soc.* **1964c**, *63*, 535.
Pressley, H.; White, J. *Trans. J. Brit. Ceram. Soc.* **1979**, *78*, 4.
Rigby, G. R.; Hamilton, B. *J. Am. Ceram. Soc.* **1961**, *44*, 201.
Rigby, G. R.; Hamilton, B. *Trans. Metall. Soc. AIME* **1962**, *224*, 887.
Trojer, F. *Radex Rundsch.* **1958**, *7*, 365.
Ust'yantsev, V. M.; Mar'evich, V. P.; Perepelitsyn, V. A. *Ogneuporv.* **1971**, *36*, 28.
Ust'yantsev, V. M.; Mar'evich, V. P.; Lapachak, G. G. *Izv. Akad. Nauk USSR, Neorg. Mater.* **1972**, *8*, 590.

Received for review May 9, 1983

Accepted April 9, 1984

Mass Transfer Due to a Confined Laminar Impinging Axisymmetric Jet

Hin-Sum Law and Jacob H. Masliyah*

Department of Chemical Engineering, University of Alberta, Edmonton, Alberta, Canada T6G 2G6

Local mass transfer due to impingement of a confined laminar axisymmetric air jet onto a flat surface has been studied both theoretically and experimentally. After release from a cylindrical tube the axis of which is perpendicular to a target plate, the jet fluid is confined to flow radially outward in a channel between two parallel plates. The range of Reynolds number was 400 to 1900 and the jet-to-plate spacings were 2 and 4 times the jet nozzle diameter. The experimental study was carried out with double exposure holography and the theoretical study was made with the numerical solution of the transport equations using an upstream-weighted differencing scheme. In general, flow separation along the impingement plate occurred at a radial distance far away from the stagnation point. It was found that the variation of the local Sherwood number is similar to that of an unconfined jet in the stagnation flow region and in the wall jet region prior to flow separation. Beyond the flow separation region, the local Sherwood number is smaller than that for an unconfined jet.

Introduction

Impinging jets of various configurations are frequently used in industrial equipment for their excellent heat and mass transfer characteristics. Drying of textiles and cooling of turbine blades are some of the important practical applications. Heat and mass transfer characteristics of impinging axisymmetric jets issuing from circular tubes have been studied rather extensively by Scholtz and Trass (1963,1970), Kapur and Macleod (1972,1974,1975), Saad et al. (1977), and Deshpande and Vaishnar (1982). The theoretical and experimental findings are well correlated in the stagnation-flow and in the wall-jet regions. However, of these studies, only the numerical study by Saad et al. (1977) considered the effect of the presence of a confinement plate, and their results were restricted in the region near the stagnation point.

The effect of the presence of a confinement plate on the mass transfer due to a laminar two-dimensional jet has been studied by Law (1982,1984). A flow separation was found along the impingement plate in the region far away from the stagnation point, producing local minimum and maximum Sherwood numbers in the separation flow region. It is commonly known that heat and/or mass transfer from axisymmetric and two-dimensional jets have similar behavior, albeit there are significant quantitative differences. The objective of the present work is to study, both experimentally and numerically, the mass transfer characteristics of a *confined* laminar axisymmetric jet impinging on a flat plate.

Table I. Coefficients of Eq 1

Φ	A_1	A_2	A_3
Ω/R	R^2	R^3/Re_d	0
Ψ	0	$1/R$	$-\Omega$
C	1	R/Re_dSc	0

Numerical Study

The impinging jet system considered in the present study is shown in Figure 1. The air jet issues from a circular tube of diameter d with an average velocity of \bar{u}_j . The confinement plate is located parallel to and at a distance h from the impingement plate. The origin of the axisymmetric coordinate system is located at the center of the jet nozzle exit. The outflow region is chosen at a location sufficiently far away from the stagnation flow region where fully developed conditions can be assumed.

The governing equations are the equations of motion in their vorticity-stream function form and the convection-diffusion equation with the assumptions of steady state and incompressible Newtonian fluid with constant physical properties. The pertinent equations can be represented by a general differential equation in the axisymmetric coordinate system as

$$A_1 \left\{ \frac{\partial}{\partial Z} \left(\Phi \frac{\partial \Psi}{\partial R} \right) - \frac{\partial}{\partial R} \left(\Phi \frac{\partial \Psi}{\partial Z} \right) \right\} - \frac{\partial}{\partial Z} \left\{ A_2 \frac{\partial \Phi}{\partial Z} \right\} - \frac{\partial}{\partial R} \left\{ A_2 \frac{\partial \Phi}{\partial R} \right\} + A_3 = 0 \quad (1)$$

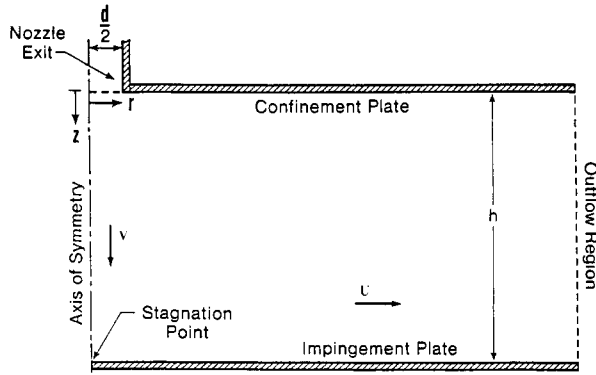


Figure 1. Coordinate system and boundaries of the jet system.

The general dependent variables Φ and corresponding coefficients A_1 , A_2 , and A_3 are listed in Table I, where Φ represents either the vorticity Ω/R , stream function Ψ , or the concentration C . The vorticity and the stream function are defined as

$$\frac{\Omega}{R} = \frac{\partial U}{\partial Z} - \frac{\partial V}{\partial R} = -\frac{1}{R^2} \left(\frac{\partial^2 \Psi}{\partial R^2} + \frac{\partial^2 \Psi}{\partial Z^2} \right) + \frac{1}{R^2} \frac{\partial \Psi}{\partial R} \quad (2)$$

$$V = \frac{1}{R} \frac{\partial \Psi}{\partial R}; \quad U = -\frac{1}{R} \frac{\partial \Psi}{\partial Z} \quad (3)$$

All the variables in eq 1-3 are dimensionless and are defined as

$$\begin{aligned} H &= h/d \\ U &= u/\bar{v}_j; \quad V = v/\bar{v}_j \\ R &= r/d; \quad Z = z/d \\ C &= (c - c_j)/(c_s - c_j) \\ \Omega &= \omega(d/\bar{v}_j); \quad \Psi = \psi/(\bar{v}_j d^2) \\ Re_d &= \bar{v}_j d/\nu; \quad Sc = \nu/D \end{aligned} \quad (4)$$

The objective of the numerical study is to solve eq 1 for Ω/R , Ψ , and C . Because the equations are elliptic in nature, boundary conditions must be specified at all the boundaries. The boundaries are specified for five regions.

1. Nozzle Exit. From the fully developed velocity profile in a circular tube, the stream function becomes

$$\Psi = R^2 - 2R^4 \quad (5)$$

$$\Omega/R = 16 \quad (6)$$

and

$$C = 0 \quad (\text{pure air at jet exit}) \quad (7)$$

2. Confinement Plate. Because the confinement plate is impermeable, the value of the stream function does not change along the plate. This value can be determined by substituting $R = 1/2$ in eq 5 to give

$$\Psi = 1/8 \quad (8)$$

The boundary condition for the vorticity at the confinement plate is approximated by a finite-difference expression which embodies the no-slip conditions ($\partial \Psi / \partial Z = 0$ and $\partial^2 \Psi / \partial Z^2 = -R\Omega$) at the boundary, together with the assumption of linearly varying vorticity near the plate. The boundary condition for the vorticity is

$$\frac{\Omega_{p1}}{R} = - \left\{ \frac{3(\Psi_{np} - \Psi_{p1})}{R^2 \Delta Z_{np}^2} + \frac{\Omega_{np}}{2R} \right\} \quad (9)$$

where the subscripts pl and np are the values of the variables at the plate and at the gridline next to it, respectively. ΔZ_{np} is the grid spacing between the np-th gridline and the plate. The boundary condition for the concentration is given by

$$\frac{\partial C}{\partial Z} = 0 \quad (\text{zero mass flux}) \quad (10)$$

3. Impingement Plate. Again, because the impingement is impermeable, the value of the stream function does not change along the plate, and its value is

$$\Psi = 0 \quad (11)$$

The boundary condition for the vorticity is the same as in eq 9. The boundary condition for the concentration is

$$C = 1 \quad (12)$$

4. Axis of Symmetry. Along the axis of symmetry the boundary conditions are

$$\Psi = 0 \quad (13)$$

$$\frac{\partial}{\partial R} \left(\frac{\Omega}{R} \right) = 0 \quad (14)$$

and

$$\frac{\partial C}{\partial R} = 0 \quad (15)$$

Because of axial symmetry, $\Omega = 0$ at $R = 0$. However, $\Omega/R \neq 0$, and Ω/R can be evaluated as follows. Assume that Ψ is of the form

$$\Psi = b_1 R^2 + b_2 R^4 \quad (16)$$

near the axis, where b_1 and b_2 are functions of Z only. At a given value of Z , the value of Ω/R can be expressed as

$$\frac{\Omega}{R} = -8b_2 - \frac{\partial^2 b_1}{\partial Z^2} \quad (17)$$

by substituting eq 16 into eq 2. The values of b_1 and b_2 can be obtained as

$$b_1 = \frac{1}{R_{sa}^2 - R_{na}^2} \left(\frac{\Psi_{sa}}{R_{sa}^2} - \frac{\Psi_{na}}{R_{na}^2} \right) \quad (18)$$

$$b_2 = \frac{1}{R_{sa}^2 - R_{na}^2} \left(\frac{R_{sa}^2}{R_{na}^2} \Psi_{na} - \frac{R_{na}^2}{R_{sa}^2} \Psi_{sa} \right) \quad (19)$$

where the subscripts na and sa indicate the values of the variables at the gridline next to and second away from the axis, respectively.

5. Outflow Region. The fully developed stream function and vorticity profiles are derived from the fully developed velocity profile for radial flow between two parallel disks given by Bird et al. (1960). The boundary conditions at the outflow region are

$$\Psi = [2(z/h)^3 - 3(z/h)^2 + 1]/8 \quad (20)$$

$$\frac{\Omega}{R} = \frac{3}{4H^2 R^2} \left\{ 1 - 2 \left(\frac{z}{h} \right) \right\} \quad (21)$$

and

$$\partial C / \partial R = 0 \quad (22)$$

The location of this boundary was chosen at $R_{\max} = 42$ for all numerical runs.

The dimensionless local skin friction factor, C_f , along the impingement plate is defined by

$$C_f = \tau_s / (0.5\rho\bar{u}_j^2) \quad (23)$$

where ρ is the fluid density and τ_s is the local shear stress at the impingement plate. Equation 23 leads to

$$C_f = -\frac{2}{Re_d} \left(\frac{\partial U}{\partial Z} \right) \bigg|_{Z=H} = -\frac{2R}{Re_d} \left(\frac{\partial \Omega}{\partial R} \right) \bigg|_{R=H} \quad (24)$$

The dimensionless local pressure is defined as

$$\Delta P = (p - p_{j|_{r=0}}) / (0.5\rho\bar{u}_j^2) \quad (25)$$

with $p_{j|_{r=0}}$, the local pressure at the center of the jet nozzle exit taken as the reference pressure. The dimensionless stagnation pressure, ΔP° , is given by

$$\Delta P^\circ = 4 - \frac{4}{Re_d} \int_0^H \left(\frac{\partial \Omega}{\partial R} \right) \bigg|_{R=0} dZ \quad (26)$$

for an initial parabolic velocity profile at the jet nozzle exit. The dimensionless local pressure along the impingement plate, $\Delta P|_{Z=H}$, can be derived from the r -component of the momentum equation along the impingement plate and is given by

$$\Delta P|_{Z=H} = \Delta P^\circ + \frac{2}{Re_d} \int_0^R \left(\frac{\partial \Omega}{\partial Z} \right) \bigg|_{Z=H} dR \quad (27)$$

The local mass transfer flux is given by

$$N = k(c_s - c_j)M_w = +DM_w \left(\frac{\partial c}{\partial z} \right) \bigg|_{z=h} \quad (28)$$

which leads to

$$Sh_d = \frac{kd}{D} = + \left(\frac{\partial C}{\partial Z} \right) \bigg|_{Z=H} \quad (29)$$

The approximation of a convection-diffusion differential equation by the upstream-weighted differencing schemes used in the present study was described in detail by Raithby and Torrance (1974) and will not be repeated here. In this analysis a nonuniform grid is used throughout the numerical computations in the present study. Due to the relatively large gradients of velocity and concentration along the impingement and the confinement plates, finer grid spacings are used adjacent to the two plates. This is particularly important for the impingement plate along which the skin friction factor and the Sherwood number are to be evaluated. Also, gridlines parallel and adjacent to the axis of symmetry are closely spaced in order to ensure accurate calculation of the variables within the stagnation flow region.

A grid network of 51×25 was used. The number of gridlines in the r direction was 51 with 9 gridlines covering the jet nozzle exit ($0 \leq R \leq 0.5$). The number of gridlines in the z direction was 25 with the grid spacing nearest to the impingement plate being $0.005d$.

The numerical procedure when using the Gauss-Seidel iteration method is similar to those given by Law (1982,1984) in his study of a confined two-dimensional jet. Convergence of the numerical results was assumed satisfactory when the maximum absolute difference between two consecutive iterations was within 5×10^{-4} for the vorticity, 10^{-6} for the stream function, and 10^{-5} for the concentration. The suitability of these convergence criteria was confirmed by numerical experimentation.

For a low Reynolds number case ($Re_d = 1$), arbitrary constant values are used as the initial guess for the stream function, vorticity, and concentration. The solution obtained for a particular value of Re_d was used as the initial

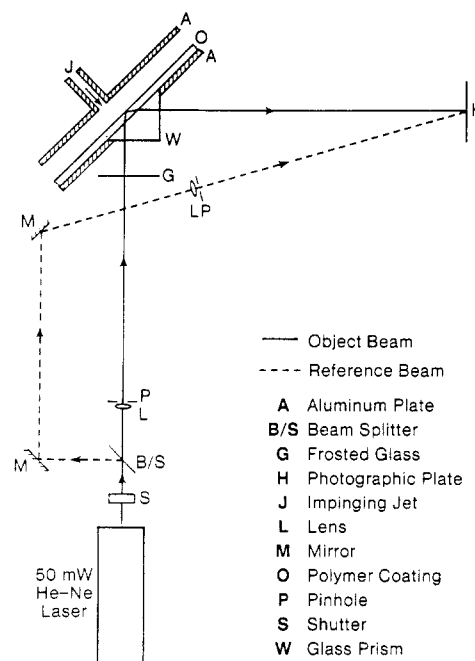


Figure 2. Arrangement of the experimental setup.

guess for a higher value of Re_d . The jet-to-plate spacings were $2d$ and $4d$.

Experimental Procedure

Kapur and Macleod (1974,1975) and Masliyah and Nguyen (1976) have demonstrated the suitability of the swollen-polymer method coupled with a laser holography interferometric technique for local mass transfer measurements. Details of this method are given by the investigators mentioned above. However, a brief description is given here. The impingement surface is made of a flat polymer coating that can be swollen by a suitable swelling agent. In the present study, ethylsalicylate is used as the swelling agent. When such a swollen polymer surface is subjected to an air jet, the swelling agent leaves the polymer surface causing local shrinkage of the polymer coating. Rate of transfer of the swelling agent from the impingement polymer surface can be evaluated from the measurements of the shrinking rate of the polymer coating. This polymer coating shrinkage is of the order of 10^{-6} m and, consequently, holographic interferometry was used to measure the change in the polymer coating thickness due to the mass transfer.

In the double exposure holographic technique, a hologram of the swollen polymer is made using a setup shown in Figure 2. Then, the coating surface is subjected to the air jet for a given duration and a second exposure is made on the original hologram. On reconstruction, the so-called "frozen fringe pattern" formed by the interference of two reconstructed images shows contours of equal surface recession or equal mass transfer.

The experimental setup and procedure, together with the zero fringe identification, are identical with the previous study of mass transfer due to a confined two-dimensional jet by Law (1982, 1984). The confinement plate is a Plexiglas plate ($0.304 \times 0.203 \times 0.012$ m) to which the circular tube jet is attached. The tube jet is 0.004 m in diameter and its length of 0.342 m is enough to provide a fully developed profile at the nozzle exit at the highest Reynolds number used in the present study.

The mass transfer experiments were conducted with the coating surface subjected to the air jet for a time, T , ranging from 90 to 480 s. The jet-to-plate spacing was $2d$ with three Reynolds numbers of 400, 950, and 1900. The

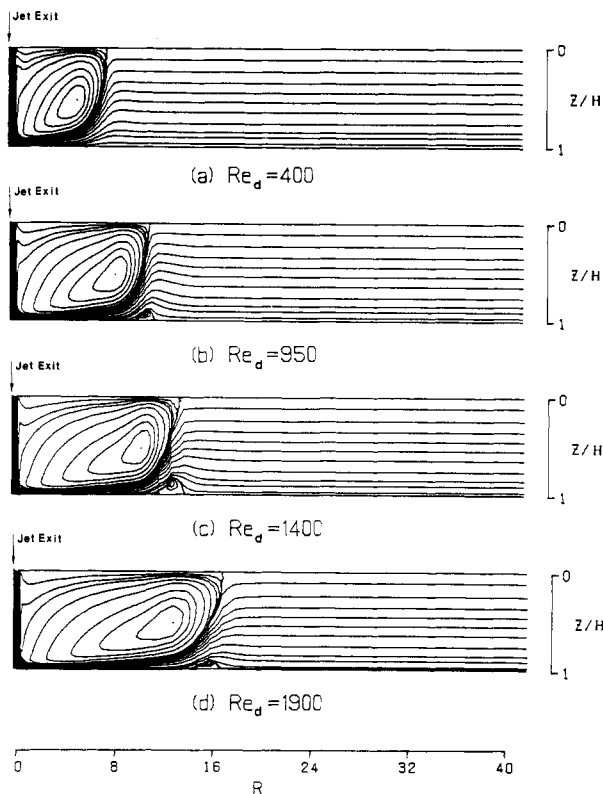


Figure 3. Contours of stream function ($H = 2$).

results of the various mass transfer experiments are presented in terms of local Sherwood number. For the present experimental setup, the local Sherwood number is given by Law (1982) as

$$Sh_d = (1.614 \times 10^{-4} P / \bar{p} p_s M_w) (n/T) (d/D) \quad (30)$$

where \bar{p} is the molar density of gas mixture, M_w is the molecular weight of the swelling agent, p_s is the swelling agent partial vapor pressure at the polymer surface, P is the total pressure, n is the fringe order, and D is the diffusion coefficient. The constant of eq 30 is a function of the optical setup, the refractive index of the coating, and its density and is given by Law (1982,1984). Therefore, from eq 30, it is necessary to know the physical properties, the local fringe order, and the duration of the mass transfer experiment in order to evaluate the local Sherwood number. The physical properties of eq 30 are given in the Appendix.

Results and Discussions

Results of two types are given: flow and mass transfer characteristics. Flow characteristics can only be studied numerically in the present work; mass transfer characteristics are studied both experimentally and numerically. Experimental results in this case are used to verify the numerical predictions.

Flow Characteristics. The flow field is studied qualitatively by observing the streamline contours. The contours of the stream function for $H = 2$ are shown in Figure 3. The jet nozzle exit is at the upper left-hand corner with the main flow traveling from left to right. The upper horizontal streamline represents the confinement plate and the lower horizontal streamline represents the impingement plate. In general, for both $H = 2$ and 4, a primary toroidal vortex rotating in the counterclockwise direction is found near the confinement plate, its size increasing with the jet Reynolds number. Except at $Re_d = 400$ for $H = 2$, a second vortex rotating in clockwise direction is also found near the impingement plate. This

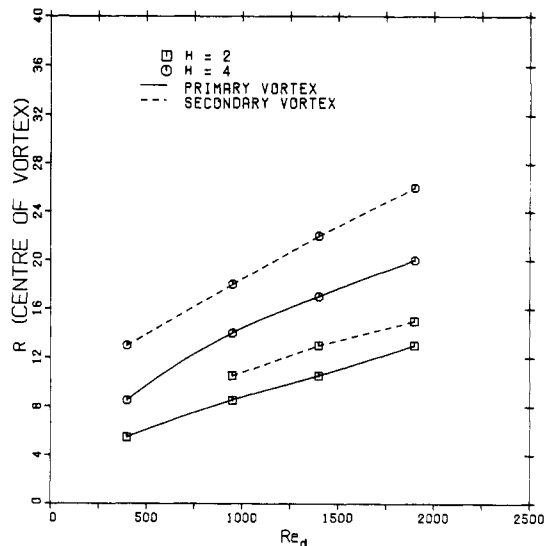


Figure 4. Variation of vortex center with Reynolds number.

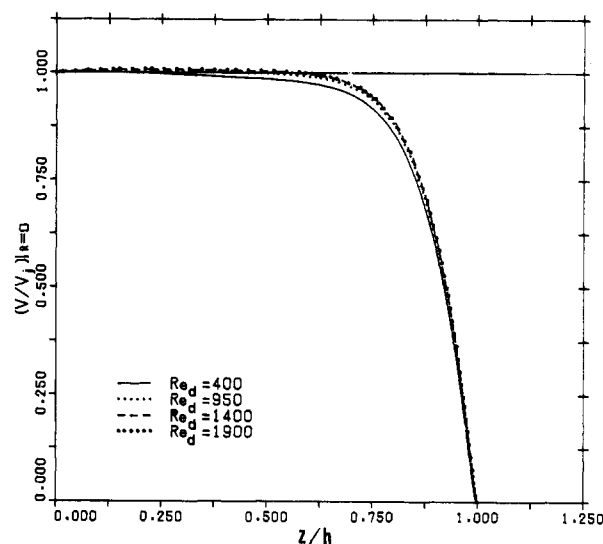


Figure 5. Decay of jet centerline axial velocity ($H = 2$).

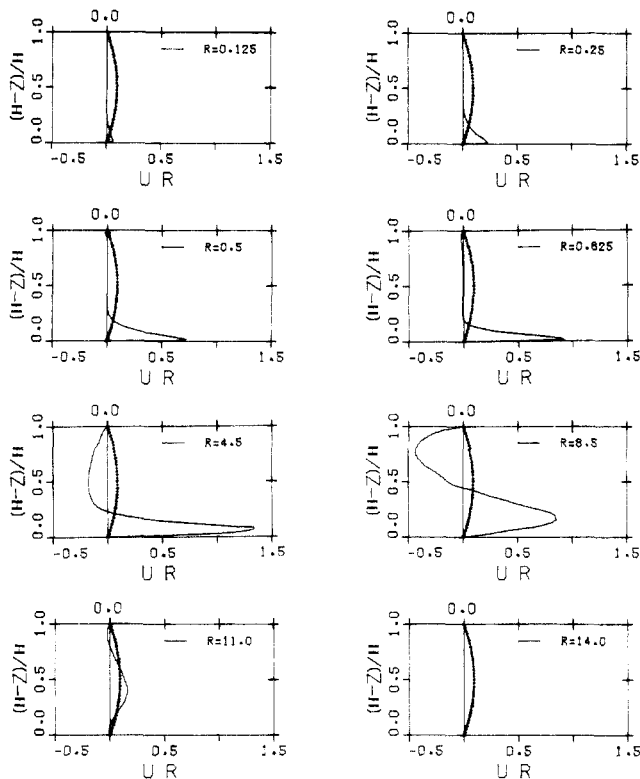
secondary vortex is much smaller than the first in size and it is also weaker in terms of rotational intensity. The variation of the location of the vortex center with the jet Reynolds number is shown in Figure 4. It can be observed that the centers of both the primary and secondary vortices move downstream with an increase in Reynolds number. From the qualitative study of the flow field, the behavior of confined axisymmetric and two-dimensional (Law, 1982, 1984) jets is very similar, but there are significant quantitative differences.

(a) Jet Centerline Axial Velocity. The decay of the jet centerline axial velocity, $V|_{R=0}$, for different jet Reynolds numbers is shown in Figure 5 for $H = 2$. The jet centerline axial velocity increases slightly with distance from the nozzle exit indicating the contraction of the jet, and then it gently decreases due to the spreading of the jet. Not until the submerged jet is about $3/4$ of the jet nozzle diameter away from the impingement plate does the jet centerline axial velocity decrease rapidly and become zero at the stagnation point. Similar behavior is also observed for the case of $H = 4$.

The effect of Reynolds number on the initial decay of the jet centerline axial velocity can also be studied from Figure 5. The jet centerline axial velocity decays less rapidly at higher Reynolds numbers. This is mostly due to the more penetration of the jet with higher Reynolds

Table II. Values of the Constant a

H	Re_d	a (from eq 31)	a (from eq 32)	\bar{a}^a
2	400	3.39	3.48	3.44
	950	3.68	3.76	3.72
	1400	3.80	3.83	3.82
	1900	3.88	3.94	3.91
4	400	3.24	3.29	3.27
	950	3.64	3.71	3.68
	1400	3.79	3.81	3.80
	1900	3.88	3.93	3.91

^a Average value of a .Figure 6. Radial velocity profiles ($H = 2$, $Re_d = 950$).

number into the surrounding fluid.

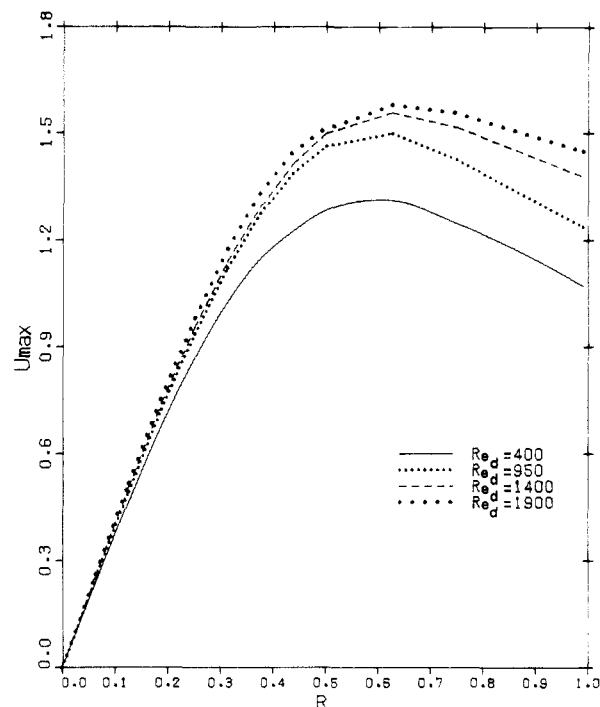
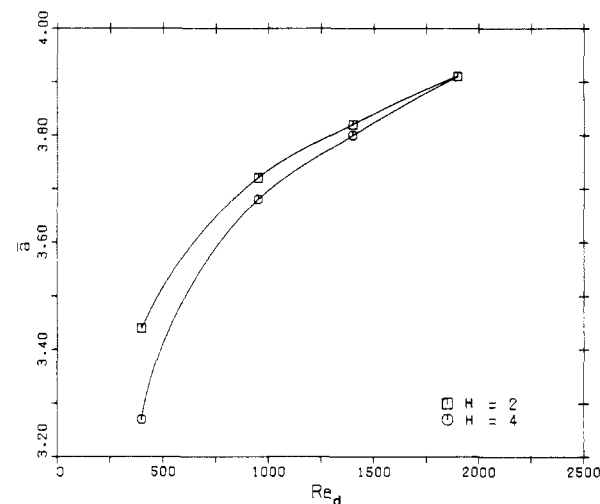
In the stagnation flow region, the jet centerline axial velocity is linearly proportional to the axial distance away from the stagnation point, $(h - z)$, as can be noted from Figure 5. This is a typical stagnation flow behavior as mentioned by Schlichting (1968). For axisymmetric stagnation flow, the jet axial velocity component is given by

$$\left(\frac{V}{V_j} \right) \bigg|_{R=0} = \frac{2aH}{(V_j)_{R=0}} \left\{ \frac{h-z}{h} \right\} \quad (31)$$

where $(V_j)_{R=0}$ is the jet centerline axial velocity at the jet nozzle exit. The values of the constant a in eq 31 can be evaluated from the slope of the curves such as those of Figure 5 and are given in Table II for both $H = 2$ and 4.

(b) Radial Velocity. Typical developments of radial velocity profiles with radial distance, R , is shown in Figure 6 for $H = 2$ and $Re_d = 950$. In Figure 6, it is noted that the radial velocity is represented by UR instead of U . In this way, a similarity velocity profile can be obtained in the fully developed flow region. The dotted line in the plots represents the similarity fully developed velocity profile at the given radial distance.

For a given radial distance close to the stagnation point, the radial velocity, U , increases from zero at the imp-

Figure 7. Variation of U_{\max} with radial distance ($H = 2$).Figure 8. Variation of \bar{a} with Reynolds number.

ingement plate to a maximum, U_{\max} , within a thin layer. Such a layer is referred to as the "viscous boundary" layer in the stagnation flow region. Outside the viscous boundary layer, the radial velocity decreases with increasing distance from the impingement plate and becomes negative in the recirculation region.

The variation of the maximum value of the radial velocity, U_{\max} , with radial distance, R , in the region of $R \leq 1$ is shown in Figure 7 for $H = 2$. In the stagnation flow region, U_{\max} is linearly proportional to the radial distance. This is a typical stagnation flow behavior shown by Schlichting (1968) in his study of axisymmetric stagnation flows. The radial velocity in the stagnation flow region is given as

$$U_{\max} = aR \quad (32)$$

It is appropriate to point out that eq 31 and 32 have the same constant, namely, a .

The values of the constant a in eq 32 can be evaluated from the slope of the curves such as those of Figure 7 and are given in Table II for both $H = 2$ and 4. Comparing the values of a from eq 31 and 32, agreement within 2.6%

Table III. Thickness of Viscous Boundary Layer in Stagnation Flow Region

H	Re_d	σ_0/d^a	σ_0/d^b
2	400	0.0435	0.0526
	950	0.0290	0.0328
	1400	0.0255	0.0267
	1900	0.0235	0.0226
4	400	0.0445	0.0539
	950	0.0290	0.0330
	1400	0.0255	0.0267
	1900	0.0235	0.0226

^a From numerical measurement. ^b From eq 33.

is obtained. The average values of the constant of eq 31 and 32, $\bar{\alpha}$, are given in Table II. A plot of $\bar{\alpha}$ as a function of Reynolds number is shown in Figure 8. It is found that for both $H = 2$ and 4, $\bar{\alpha}$ increases with Reynolds number.

The thickness of the viscous boundary layer in the stagnation flow region, σ_0 , is defined as the distance from the impingement plate where the radial velocity reaches 99% of U_{\max} . This boundary layer thickness, which is nearly constant throughout the stagnation flow region, can be determined from the radial velocity profiles in the stagnation flow region. The measured values of σ_0/d are given in Table III.

On the other hand, the thickness of the viscous boundary layer in the stagnation flow region can also be predicted for high Reynolds numbers from the value of $\bar{\alpha}$ using the equation given by Schlichting (1968) in his study of axisymmetric stagnation flow as

$$\sigma_0/d = 1.95/(\bar{\alpha}Re_d)^{0.5} \quad (33)$$

By using the value of $\bar{\alpha}$ in Table II, the values of σ_0/d evaluated from eq 33 are also given in Table III. Good agreement was obtained for the boundary layer thickness for high Reynolds numbers using the two approaches. The prediction of eq 33 becomes less accurate at lower value of Reynolds numbers. It appears that Schlichting's analysis in the stagnation flow region for the axisymmetric flow is applicable at high Reynolds numbers to the present study where a *confined jet* is used.

(c) **Skin-Friction Factor.** The variation of local skin-friction factor near the stagnation flow region is shown in Figure 9 for $H = 2$ as a plot of $0.5C_fRe_d^{0.5}$ vs. R . In general, the local skin-friction factor increases sharply from zero at the stagnation point to a maximum value in a short distance and then decreases with radial distance, R . The location of the maximum value is found near $R = 0.5$ for both $H = 2$ and 4. This location of the maximum value agrees with the observation by Saad et al. (1977) for a "semi-confined" axisymmetric jet. Their results are obtained at $Re_d = 450, 950$, and 1960 for $H = 8$.

Eventually, C_f should approach the value of that of the fully developed profile between two parallel disks. For fully developed flow between two parallel disks, the skin-friction factor is given by

$$(C_f)_{fd} = 3/(2H^2RRe_d) \quad (34)$$

Therefore, a plot of C_fRe_dR vs. R for a given jet-to-plate spacing leads to the collapse of all curves for different Reynolds numbers to a single curve in the region far away from the stagnation point. Variation of C_fRe_dR vs. R is shown in Figure 10 for $H = 2$. A general curve approaching the constant value of $3/2H^2$, which is equal to 0.375 for $H = 2$, is obtained for the different Reynolds numbers. This indicates the existence of a fully developed flow region between the impingement and confinement plates as would be expected.

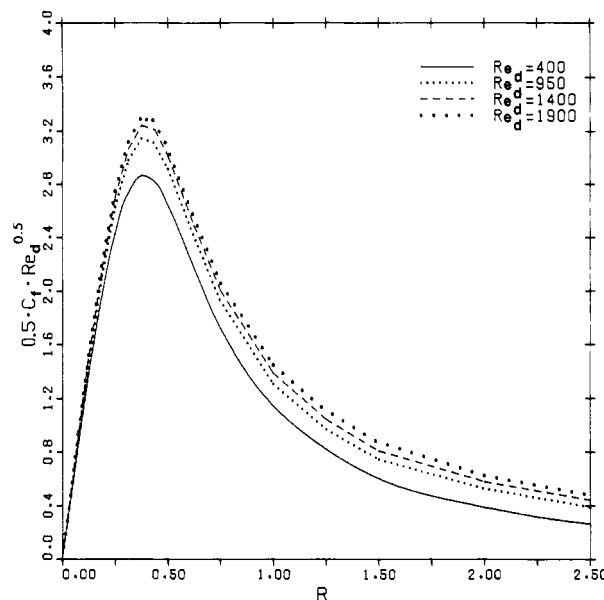


Figure 9. Variation of local skin-friction factor near the stagnation flow region ($H = 2$).

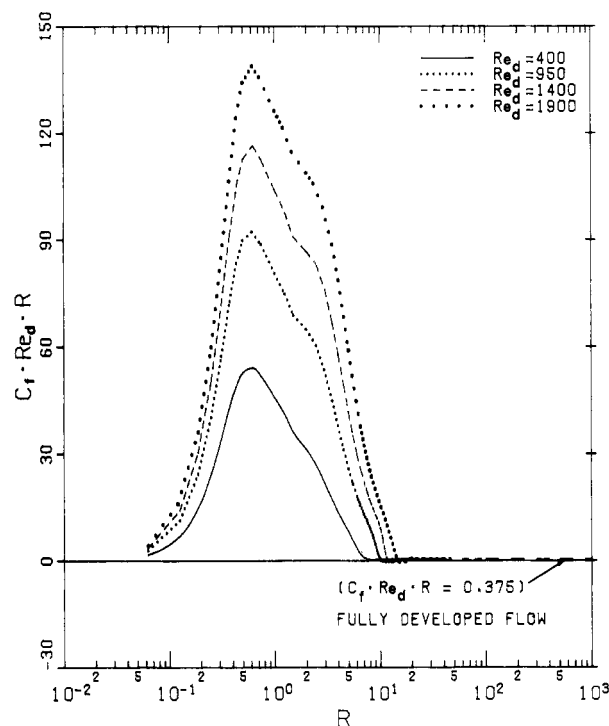


Figure 10. Variation of local skin-friction factor ($H = 2$).

(d) **Pressure Distribution along the Impingement Plate.** Figure 11 shows the impingement plate pressure distribution near the stagnation point. The maximum local pressure is found to occur at the stagnation point and it decreases monotonically from its maximum value. Also shown in Figure 11 are the theoretical and experimental results given by Scholtz and Trass (1970) for an unconfined laminar axisymmetric jet. There is excellent agreement between their results and those of the present study.

The stagnation pressure, ΔP^0 , is plotted as a function of Reynolds number in Figure 12 for both $H = 2$ and 4. For a given jet-to-plate spacing ΔP^0 increases with Reynolds number and it is less than the value of 4 for an inviscid flow as is indicated by eq 26.

Mass Transfer Characteristics. The variations of the calculated local Sherwood number along the impingement plate for different Reynolds numbers and jet-to-plate

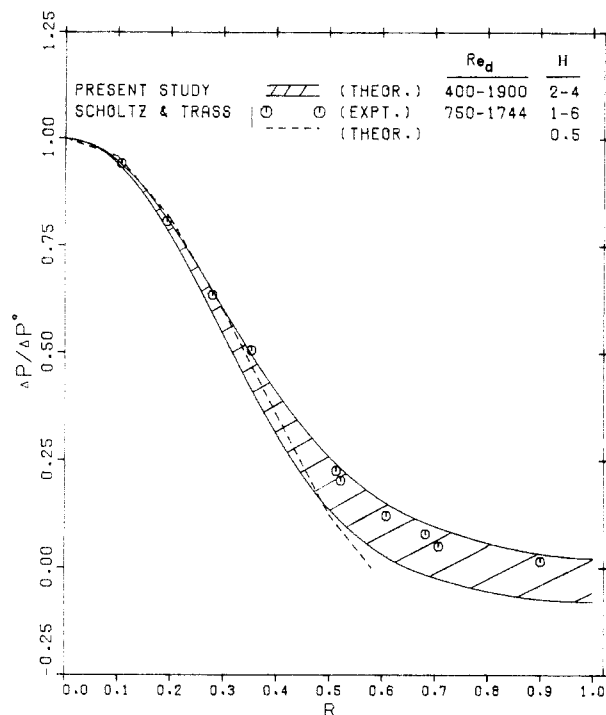


Figure 11. Variation of local pressure along the impingement plate in the stagnation flow region.

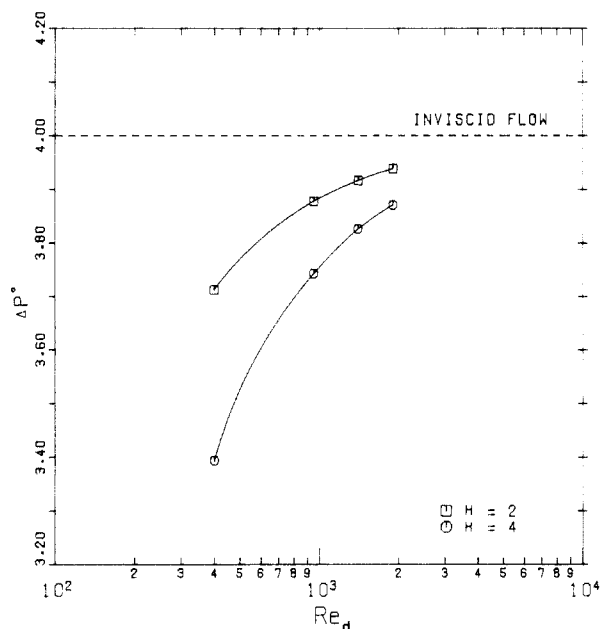


Figure 12. Stagnation pressure as a function of Reynolds number.

spacings are shown in Figure 13 using the computer results. It is noted that for a given Reynolds number the local Sherwood number is independent of jet-to-plate spacing in the stagnation flow and the wall jet regions. This confirms the findings by Scholtz and Trass (1970) for an unconfined axisymmetric jet. They have stated that there is no effect of jet-to-plate spacing on mass transfer due to an unconfined impinging axisymmetric jet for $0.25 \leq H \leq 6$. On the other hand, Figure 13 shows that the effect of jet-to-plate spacing on the local Sherwood number becomes significant only at a radial distance just prior to and beyond the flow separation along the impingement plate.

For all cases, the maximum Sherwood number is found to occur close to the stagnation point. Comparison of the stagnation point Sherwood numbers evaluated numerically with those in the literature is shown in Figure 14. The

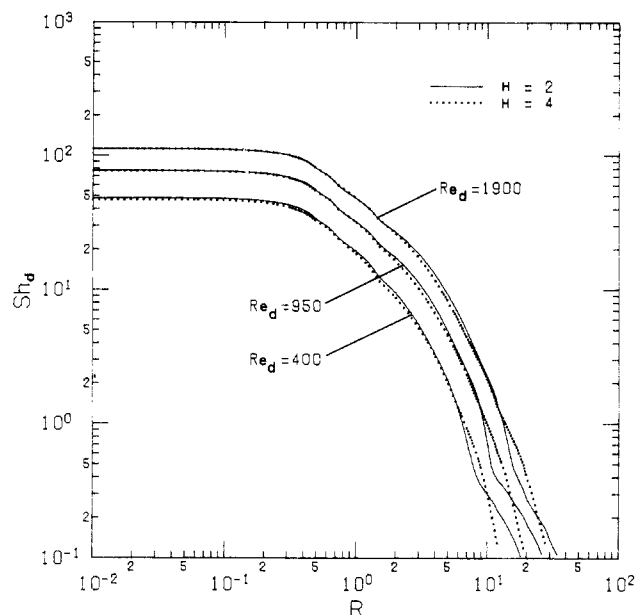


Figure 13. Variation of local Sherwood number.

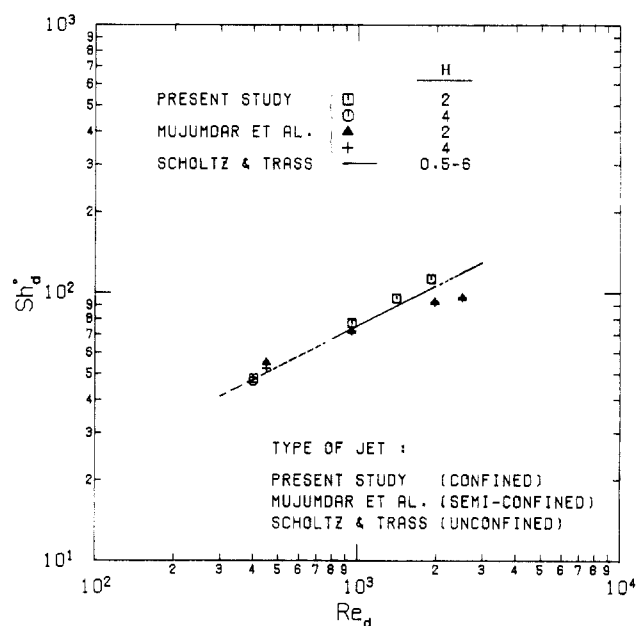


Figure 14. Comparison of stagnation point Sherwood number with literature ($Sc = 2.74$).

heat transfer results of Saad et al. (1977) for a "semi-confined" jet were converted to the corresponding mass transfer values by employing a heat-mass transfer analogy, where $Sh_d = (Sc/Pr)^{0.4} Nu_d$. The mass transfer results of Scholtz and Trass (1970) for an unconfined jet are evaluated by using their correlation, given by

$$Sh_d^\circ = 1.6484 Re_d^{0.5} Sc^{0.361} \quad (35)$$

for $800 \leq Re_d \leq 1970$ and $0.5 \leq H \leq 6$. Extrapolated data of this correlation are shown as a dashed line in Figure 14. Close agreement between the results from the present study and those from Scholtz and Trass (1970) indicates that there is little effect on the stagnation point mass transfer due to the presence of a confinement plate.

In the present study, the objective of the experimental study is to verify the numerical predictions. A typical "frozen fringe pattern" due to mass transfer from a flat plate under the influence of a confined laminar axisymmetric jet for $T = 120$ s, $Re_d = 950$, and $H = 2$ is shown in Figure 15. In Figure 15, the outer bright region is

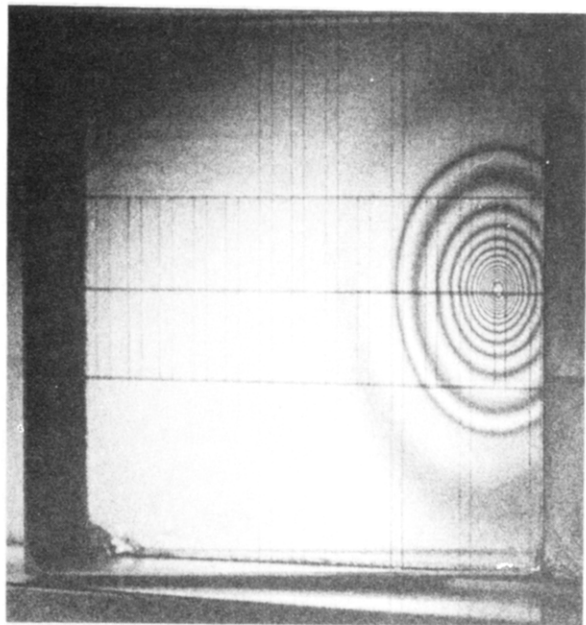


Figure 15. Contour of equal mass transfer rate ($H = 2$, $Re_d = 950$).

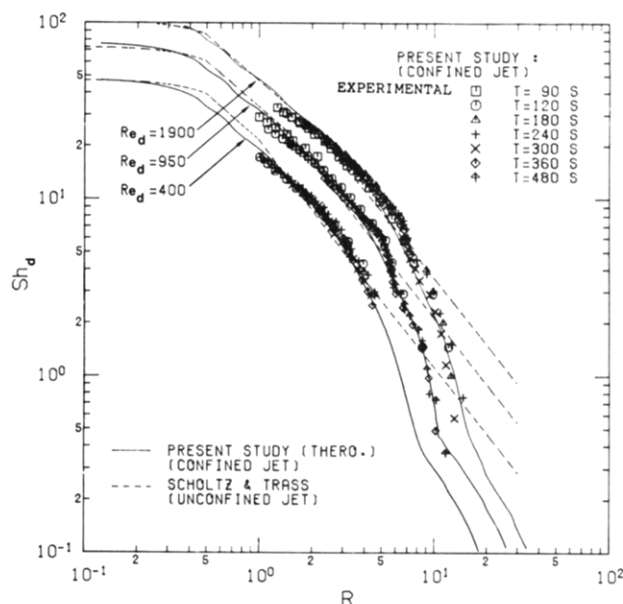


Figure 16. Comparison of experimental and numerical results.

considered to be the zeroth-order fringe where no mass transfer has occurred. By counting the fringe order from the outer zeroth-order fringe toward the stagnation point, it is possible to label all the fringes. After the local fringe order is determined, the local Sherwood number can then be evaluated by using eq 30.

Comparisons between the experimental (shown as symbols) and the numerical results are shown in Figure 16. Excellent agreement is obtained between the experimental and the numerical results. Also shown in Figure 16 are the distributions of local Sherwood number given by Scholtz and Trass (1963, 1970) for an unconfined axisymmetric jet.

It is found that the variation of the local Sherwood number for a confined axisymmetric jet is similar to that of an unconfined jet in the stagnation flow region and in the wall jet region prior to flow separation. Due to the good agreement between Scholtz and Trass results for the unconfined jet with the present study for the confined jet, it suffices to give their correlations casted for $Sc = 2.74$ as

$$Sh_d/Re_d^{0.5} = 2.372 - 1.595R^2 + \dots \quad (36)$$

in the stagnation flow region ($R \leq 0.5$)

$$Sh_d/Re_d^{0.5} = 1.087R^{-0.86} \quad (37)$$

in the transition region ($0.5 \leq R \leq 2.25$), and

$$Sh_d/Re_d^{0.75} = 0.224R^{-1.25} \quad (38)$$

in the wall jet region ($R \geq 2.25$).

Beyond the flow separation region, the local Sherwood number is smaller than that for an unconfined jet. Sharp decrease of the local Sherwood number in the flow separation region was also observed by Law (1982, 1984) in his study of a confined two-dimensional jet. In the flow separation region of a *confined two-dimensional* jet, the local Sherwood number decreases sharply at first, but eventually recovers to exhibit a local minimum and a local maximum. In the flow separation region of a *confined axisymmetric* jet, no recovery of the local Sherwood number is found and therefore no local extrema exist. In this region, $\log(Sh_d)$ decreases rather linearly with $\log(R)$ as shown in Figure 16. Eventually in the outflow region, the local Sherwood number approaches zero.

A regression equation is developed from the experimental data for $H = 2$ in the flow separation region. The regression analysis is made in such a way that each data point has approximately the same weighting.

The regression equation is given by

$$Sh_d/Re_d^{1.39} = 0.038R^{-2.79} \quad (39)$$

for $R \geq 5$, $400 \leq Re_d \leq 1900$, $H = 2$ and $Sc = 2.74$ with an average error of 12%. A total of 90 data points are used.

Concluding Remarks

The local Sherwood number along the impingement plate for a confined axisymmetric jet is found to behave quite similarly to that for an unconfined jet except in the region far away from the stagnation point. In this region, the local Sherwood number is smaller than that for an unconfined jet mainly because of the flow separation along the impingement plate. A numerical model with upstream-weighted differencing scheme is found to be very successful in predicting the mass transfer due to a confined laminar impinging axisymmetric jet.

Acknowledgment

The authors are indebted to the Natural Sciences and Engineering Research Council of Canada for financial support.

Appendix

Molecular weight of ethylsalicylate, $M_w = 166.17$ kg/kmol

Vapor pressure of ethylsalicylate, p_s (at 21 °C and 93.7 kPa) = 0.00843 kPa

Molar density of gas mixture, \bar{p} (at 21 °C and 93.7 kPa) = 0.0383 kmol/m³

Diffusion coefficient, D (at 21 °C and 93.7 kPa) = 6.0×10^{-6} m²/s

Schmidt number of ethylsalicylate-air system, Sc (at 21 °C) = 2.74

Nomenclature

a = constant in eq 31 and 32

A_1, A_2, A_3 = coefficients in eq 1

\bar{a} = average value of the constants a in eq 31 and 32

b_1, b_2 = coefficients in eq 16

c = concentration of swelling agent, kmol/m³

C = dimensionless concentration of swelling agent, $(c - c_j)/(c_s - c_j)$

C_f = skin-friction factor, $\tau_s/(0.5\rho\bar{v}_j^2)$

d = nozzle diameter, m

D = diffusion coefficient, m^2/s
 h = jet-to-plate spacing, m
 H = dimensionless jet-to-plate spacing, h/d
 k = local mass transfer coefficient defined in eq 28, m/s
 M_w = molecular weight of swelling agent, kg/kmol
 n = fringe order
 N = mass flux, $\text{kg/m}^2 \text{ s}$
 p = pressure, kPa
 p_s = partial vapor pressure of swelling agent at the polymer surface, kPa
 P = total pressure, kPa
 Pr = Prandtl number
 r = radial distance measured from the jet center, m
 R = dimensionless radial distance, r/d
 Re_d = Reynolds number, $\bar{v}_j d/\nu$
 Sc = Schmidt number, ν/D
 Sh_d = Sherwood number, kd/D
 Sh_d^o = stagnation point Sherwood number
 T = duration of mass transfer experiment, s
 u = radial velocity, m/s
 U = dimensionless radial velocity, u/\bar{v}_j
 U_{\max} = maximum value of dimensionless radial velocity for an individual radial velocity profile
 v = axial velocity, m/s
 \bar{v}_j = average velocity of jet at nozzle exit, m/s
 V = dimensionless axial velocity, v/\bar{v}_j
 z = axial distance measured from the jet center, m
 Z = dimensionless axial distance, z/d

Greek Letters

ΔP = dimensionless pressure difference, $(p - p_j|_{r=0})/(0.5\rho\bar{v}_j^2)$
 ΔP^o = dimensionless stagnation pressure
 ΔZ_{np} = grid spacing in Z direction measured between the confinement or the impingement plate and the gridline next to it
 ν = kinematic viscosity of fluid, m^2/s
 ρ = density of fluid, kg/m^3
 $\bar{\rho}$ = molar density of gas mixture, kmol/m^3

σ_0 = viscous boundary layer thickness in stagnation flow region, m
 τ_s = shear stress at impingement plate, N/m^2
 ψ = stream function, m^3/s
 Ψ = dimensionless stream function, $\psi/(d^2\bar{v}_j)$
 ω = vorticity, s^{-1}
 Ω = dimensionless vorticity, $\omega(d/\bar{v}_j)$

Subscripts

d = nozzle diameter as characteristic length
 fd = fully developed flow
 j = at jet nozzle exit
 \max = maximum value
 na = at gridline nearest and parallel to the axis of symmetry
 np = at gridline nearest and parallel to the confinement or the impingement plate
 pl = at the confinement or the impingement plate
 s = at coating surface or impingement plate
 sa = at gridline second away from and parallel to the axis of symmetry

Literature Cited

- Bird, R. B.; Stewart, W. E.; Lightfoot, E. N. "Transport Phenomena"; Wiley: New York, 1960; p 114.
 Deshpande, M. D.; Vaishnav, R. M. *J. Fluid Mech.* **1982**, *114*, 213.
 Kapur, D. N.; Macleod, N. *Nature Phys. Sci.* **1972**, *237*, 57.
 Kapur, D. N.; Macleod, N. *Int. J. Heat Mass Transfer* **1974**, *17*, 1151.
 Kapur, D. N.; Macleod, N. *AIChE J.* **1975**, *21*, 184.
 Law, H. S. Ph.D. Dissertation, University of Alberta, Edmonton, Alberta, 1982.
 Law, H. S.; Masliyah, J. H. *Int. J. Heat Mass Transfer* **1984**, *27*, 529.
 Masliyah, J. H.; Nguyen, T. T. *Can. J. Chem. Eng.* **1976**, *54*, 299.
 Rathby, G. D.; Torrance, K. E. *Comput. Fluids* **1974**, *2*, 191.
 Saad, N. R.; Douglas, W. J. M.; Mujumdar, A. S. *Ind. Eng. Chem. Fundam.* **1977**, *16*, 148.
 Schlichting, H. "Boundary Layer Theory", 6th ed., McGraw-Hill: New York, 1968; p 92.
 Scholtz, M. T.; Trass, O. *AIChE J.* **1963**, *9*, 548.
 Scholtz, M. T.; Trass, O. *AIChE J.* **1970**, *16*, 82.
 Scholtz, M. T.; Trass, O. *AIChE J.* **1970**, *16*, 90.

Received for review May 23, 1983

Accepted February 21, 1984

Correlation of Second Virial Coefficients Using a Modified Cubic Equation of State

Joseph J. Martin*

Department of Chemical Engineering, The University of Michigan, Ann Arbor, Michigan 48109

The cubic equation of state (eq 4) is shown to be well suited to represent the generalized second virial coefficient, BP_c/RT_c , as a function of the reduced temperature. The range of application is for T_r between 0.5 and 2.0, with the temperature function, T_r^n , being modified slightly to $T_r^n - \alpha e^{-\beta T_r}$ for the lowest temperatures. For a wide variety of substances, the equation correlates the virial coefficient data to within the average precision of different investigators.

Scope

The correlating function for the generalized second virial coefficient, which follows from the cubic equation of state with the modified temperature function, is

* This author is deceased. Final corrections were made by his faculty colleague, Dr. Robert H. Kadlec, to whom correspondence should be addressed (Department of Chemical Engineering, University of Michigan, Ann Arbor, MI 48109).

$$\frac{BP_c}{RT_c} = \frac{bP_c}{RT_c} - \frac{27/64}{T_r(T_r^n - \alpha e^{-\beta T_r})}$$

If the reduced temperature does not go below 0.8, the term $\alpha e^{-\beta T_r}$ may be dropped without appreciably affecting the results. The equation has been applied to a dozen substances carefully chosen for their wide range of the critical compressibility factor, Z_c , and the slope, M , of the vapor pressure at the critical point. The equation constants for